Limited Dust Settling in the Edge-on Class I Disk IRAS 04302+2247

Zhe-Yu Daniel Lin[1]
Advisor: Zhi-Yun Li[1]
[1]*Department of Astronomy, University of Virginia, 530 McCormick Rd., Charlottesville 22904, Virginia, USA*

ABSTRACT

While dust disks around optically visible, Class II protostars are found to be vertically thin, when and how dust settles to the midplane is unclear. As part of the Atacama Large Millimeter/submillimeter Array (ALMA) large program, Early Planet Formation in Embedded Disks (eDisk), we analyze the edge-on, embedded, Class I protostar IRAS 04302+2247, also nicknamed the “Butterfly Star". With a resolution of 0.05′′ (8 au), the 1.3 mm continuum shows an asymmetry along the minor axis which is evidence for an optically thick and geometrically thick disk viewed nearly edge-on. There is no evidence of rings and gaps, which could be due to the lack of radial substructure or the highly inclined and optically thick view. Through forward ray tracing using RADMC3D, we find that the dust scale height is ∼ 6 au at a radius of 100 au from the central star and is comparable to the gas pressure scale height. The results suggest that the dust of this Class I source has yet to vertically settle significantly.

1 INTRODUCTION

The formation of rotationally supported circumstellar disks plays a crucial role in the star and planet formation process. As a consequence of the conservation of angular momentum, much of the material from the larger scale core is channeled to the disk and subsequently accretes onto the protostar itself (e.g. Terebey et al. 1984; Li et al. 2014; Tsukamoto et al. 2022). The reservoir of material in the disk enables the growth of solids and serves as the birthplace of planets (e.g. Testi et al. 2014; Drazkowska et al. 2022; Tu et al. 2022). Nevertheless, the process of dust evolution, from sub-micron sized particles inherited from the core to planetesimals and planets, requires numerous mechanisms to overcome multiple growth barriers, e.g., the meter-sized barrier (Weidenschilling 1977). One of the most favored mechanisms to overcome the meter-sized barrier is the streaming instability, which can drive rapid growth from pebbles to planetesimals, but it requires comparable densities of the dust and the gas rather than the 1:100 dust-to-gas ratio inherited from the interstellar medium (e.g. Youdin & Goodman 2005; Lesur et al. 2022). One natural process to increase the dust-to-gas ratio is through dust settling (e.g. Gole et al. 2020).

Gaseous disks are vertically extended due to the vertical pressure support. The balance between pressure gradient and the vertical gravitational pull sets the gas scale height. In contrast, dust particles, if decoupled from the pressure supported gas, will inevitably descend to the midplane to form a thin dust layer. Turbulent mixing operates against dust settling by stirring up the dust and prevents the dust from becoming fully settled (e.g. Nakagawa et al. 1986; Dubrulle et al. 1995). While the tendency for settling is well established, the effectiveness of turbulence is not clear and relies on observations for constraints (e.g. Pinte et al. 2016; Ohashi & Kataoka 2019; Villenave et al. 2022). However, observations that can characterize the vertical structure of disks are few in number, since it requires high angular resolution of nearly edge-on disks (Tobin et al. 2010; Sakai et al. 2017; Lee et al. 2017, 2020; Villenave et al. 2020; Ohashi et al. 2022; Michel et al. 2022).

IRAS 04302+2247 (hereafter IRAS 04302) is a Class I (bolometric temperature $T_{\rm bol}$ = 88 K; Ohashi et al. prep) protostar, poetically nicknamed the “Butterfly Star" by Lucas & Roche (1997) for its remarkable bipolar reflection nebulae in the near-infrared. High-resolution near-infrared images from the Hubble Space Telescope/NICMOS exhibited a clear dark lane sandwiched between the reflection nebulae and depicts a highly inclined system with an obscured central source and bipolar cavity walls that scatter the near-infrared photons (Padgett et al. 1999). A molecular outflow in H_2 was detected in the same direction as the bipolar cavity walls (Lucas & Roche 1998), and the deep absorption silicate feature in the mid-infrared requires significant inclination (Furlan et al. 2008). Indeed, millimeter wavelength observations show an elongated continuum within the near-infrared dark lane which is evidence of the presence of an edge-on disk (Wolf et al. 2003, 2008; Sheehan & Eisner 2017; van't Hoff et al. 2020; Villenave et al. 2020).

Detailed models of IRAS 04302 using scattered light images and the mm-continuum images, which trace different physical processes and regions of the circumstellar system, have ascertained an inclined system of a disk and envelope (e.g. Wolf et al. 2003, 2008; Furlan et al. 2008; Eisner 2012; Sheehan & Eisner 2017). Intriguingly, the dust in the envelope is consistent with interstellar medium (ISM) grains (e.g. Lucas & Roche 1997), while the dust in the disk is found to have grown significantly (Wolf et al. 2003; Gräfe et al. 2013; Sheehan & Eisner 2017). Furthermore, Gräfe et al. (2013) suggested that the larger grains in the disk show evidence of radial and vertical decoupling from the small grains.

Recent molecular line observations with ∼ 0.3′′ to 0.4′′ achieved by ALMA have begun to resolve the locations where molecules trace the disk surface, making the study of its vertical structure possible (van't Hoff et al. 2020; Podio et al. 2020). van't Hoff et al. (2020) identified $C^{17}O$ in the midplane within 100 *au* and detected emission in the disk surface layers beyond 100 *au* which can be explained by freeze-out of CO. In addition, H_2CO $(3_{1,2} - 2_{1,1})$ mainly originates from the disk surface layers with a large reduction of emission at the midplane where the continuum is located. Podio et al. (2020) also found a similar distribution of emission for ^{12}CO $(2-1)$, H_2CO

($3_{2,1} - 2_{1,1}$), and CS (5 − 4). The pattern is consistent with results from thermo-chemical models that consists of a midplane freeze-out and an elevated molecular layer separated by a snow surface (e.g. Aikawa et al. 2002; Akimkin et al. 2013; Dutrey et al. 2014).

Most of the prior continuum observations have been limited in angular resolution with ∼ 0.2″ to 0.5″ making it difficult to resolve the vertical structure of the dust (Gräfe et al. 2013; van't Hoff et al. 2020; Podio et al. 2020). The highest angular resolution of the continuum to date is ∼ 0.06″ at λ = 2.1 mm and hints at a flared dust disk (Villenave et al. 2020). The unique view of IRAS 04302 thus serves as a perfect laboratory to study the vertical structure of the dust and gas around a young source in detail. As part of the Early Planet Formation in Embedded Disks (eDisk) program, we present high-resolution λ = 1.3 mm continuum (∼ 0.05″ or 8 au) and molecular line images (∼ 0.1″ or 16 au) obtained from ALMA.

IRAS 04302 is located within the L1536 cloud of the Taurus star-forming region. The whole Taurus star-forming region is conventionally assumed to have a distance of 140 pc (Kenyon et al. 1994), but recent parallax measurements found significant depth effects for each cloud. From Gaia, Luhman (2018) and Roccatagliata et al. (2020) found a distance of 161 pc and 160.3 pc respectively for the L1536 cloud. Galli et al. (2018) inferred a distance of 162.7 pc using astrometry from the Very Long Baseline Array. For this paper, we adopt a distance of 160 pc.

The rest of the paper is organized as follows. Section 2 describes the observations and data processing, while Section 3 shows the resulting dust continuum images and molecular line channel maps. We analyze the continuum in more detail in Section 4. We discuss several implications in Section 5 and conclude in Section **??**.

2 OBSERVATIONS

The data are obtained as part of the ALMA Large Program (2019.1.00261.L, PI: N. Ohashi). The details of the survey, including the spectral setup, calibrators, and imaging procedure, are discussed in Ohashi et al. (prep). We briefly describe the relevant setup for IRAS 04302. The short baseline data of IRAS 04302 were observed on Dec. 21, 2021 in configuration C-6 with baselines ranging from 15 m to 3.6 km with an on-source integration time of ∼ 35 minutes. The long baseline data were observed on Sept. 30 and Oct. 1 in 2021 with total integration times of ∼ 2.16 hours in configuration C-8 with baselines ranging from 70 m to 11.9 km. The spectral setup was in Band 6 with a representative wavelength of 1.3 mm (225 GHz) for the continuum.

All calibration and imaging tasks utilized the Common Astronomy Software Applications (CASA) package (McMullin et al. 2007) version 6.2.1 and pipeline version 2021.2.0.128. From the pipeline calibrated data, we follow the self-calibration procedure presented in Ohashi et al. (prep) which we briefly describe in the following. First, we image each execution block separately and align the peaks to a common phase center using the `fixvis` and `fixplanets` tasks. Second, to adjust for flux calibration uncertainties between each execution block, we scale the amplitude of the visibilities which were azimuthally binned as a function of uv-distance. We self-calibrate the short-baseline data through three rounds of phase-only calibration. With the self-calibrated short-baseline data, we include the long-baseline data and conducted one round of phase-only calibration with a solution interval that was the length of each execution block.

We used the `tclean` task to image the self-calibrated visibilities. The continuum imaging used several Briggs robust weightings from robust=-2 to 2 (Briggs 1995). Smaller robust values shows the image with better angular resolution at the expense of increased noise, while larger robust values show the image with better sensitivity albeit with lower angular resolution(e.g. Briggs 1995; Czekala et al. 2021). We adopt the image with robust=0.5 as the representative image to compromise between spatial resolution, sensitivity, and image fidelity.

The self-calibration solutions were applied to the measurement set used for the lines and further continuum subtracted using the `uvcontsub` task. Each line image cube used a robust of 0.5 and 2 with the `uvtaper` set at 2000kλ (or ∼ 0.09″). The self-calibration and imaging scripts for this source can be found at `http://github.com/jjtobin/edisk`. We assume a 10% absolute flux calibration uncertainty, but we only consider the statistical uncertainty for the rest of this paper. The resulting resolution is ∼ 0.05″ and the noise level is $\sigma \sim 1.45 \times 10^{-2}$ mJy beam^{-1}.

3 RESULTS

Fig. 1 shows the 1.3 mm continuum image with robust=0.5 and reveals a highly elongated structure which is consistent with past low angular resolution images at millimeter wavelengths (Wolf et al. 2003, 2008; Gräfe et al. 2013). The image has a peak of 1.11 mJy beam^{-1} with a noise level of σ =14.5 μJy beam^{-1}. The total flux is 184.15 mJy by integrating the emission above 3σ. The image appears largely symmetric along the major axis, but clearly asymmetric along the minor axis in which the east side is brighter than the west side. The elongated emission is expected from an inclined disk-like structure and the kinematic analysis from Lin et al. (prep) confirms a Keplerian disk. Thus, we will refer to the elongated continuum as simply the (dust) disk. Even with the higher angular resolution compared to previous observations, there is no clear evidence of rings or gaps.

To characterize the continuum image, we fit the disk with a 2D Gaussian using the CASA task `imfit`. The coordinate center of the 2D Gaussian is one of the free parameters and we get the best fit value of (04:33:16.50, +22:53:20.2) in ICRS, which we set as the origin of the image hereafter unless explicitly stated otherwise. We treat the center as the location of the star. The deconvolved full width at half maximum (FWHM) for the major and minor axes are 2.149″ ± 0.007″ and 0.2385″ ± 0.0007″ respectively. Assuming a completely flat disk, the ratio between the minor and major axes equals $\cos i$ where i is the inclination of the disk ($i = 0°$ means face-on). With the FWHM from the 2D Gaussian fitting, we derive $i \sim 84°$. Since the disk has a finite vertical thickness, the inclination estimation is a lower limit (see Section 4). The position angle (PA) of the major axis of the best fit 2D Gaussian is 174.77° ± 0.03° which we adopt as the position angle of the major axis of the system. The total flux from the fitting is 182.6 ± 0.6 mJy (1σ uncertainty).

Fig. 2 compares the major and minor axis cuts with the origin set at the center determined from the fitted 2D Gaussian. The cuts are produced by interpolating the image and we also calculate the brightness temperature T_b using:

$$T_b = \frac{h\nu}{k} \frac{1}{\ln(\frac{2h\nu^3}{c^2 J_\nu} + 1)}. \quad (1)$$

The brightness temperature is low across the disk with only ∼ 14 K at the peak. For comparison, the peak brightness temperatures at λ = 0.9 mm (ALMA Band 7) and λ = 2.1 mm (ALMA Band 4) are 10 and 6.7 K respectively (Villenave et al. 2020). The slightly higher peak brightness temperature presented here is likely because the disk is better resolved. The extent of the major axis reaches up to ∼ 2″ (320 au) from the center which is similar to the Bands 4 and

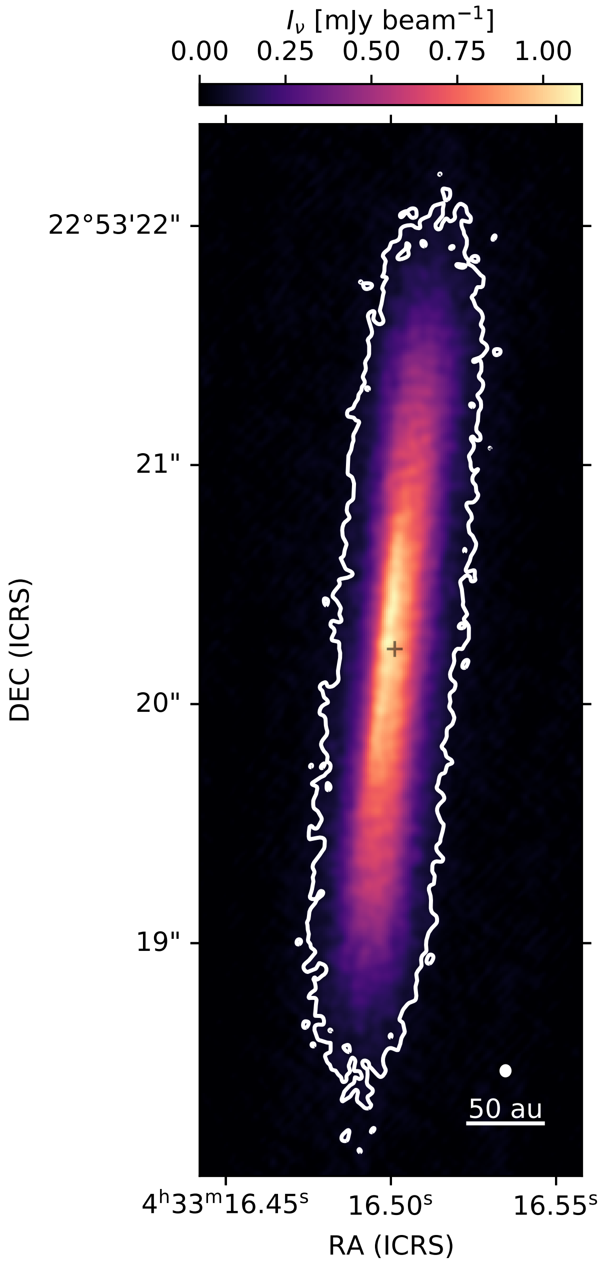

Figure 1. The continuum image of IRAS 04302+2247. The white contour marks the 5σ level. The white ellipse in the lower right is the beam size and the length scale is 50 au. The black cross marks the center from the best fit 2D Gaussian.

7 continuum images from Villenave et al. (2020). The large extent implies a fairly large disk radius which we constrain in Section 4.

To see the asymmetry along the minor axis clearly, we zoom-in on the minor axis cut and show a comparison with the beam in the right panel of Fig. 2. The FWHM of the minor axis is resolved by ~ 3.5 beams. The asymmetry could be due to an asymmetric disk or due to a highly inclined axisymmetric disk that is optically thick and not seen exactly edge-on. We favor the latter possibility since the asymmetry occurs along the minor axis and is readily consistent with the high inclination and with the direction of the outflow (Lin et al. prep). Given that the emission is brighter on the east side, we can infer that the east side is the far side of the disk based on simple expectations of an optically thick disk with decreasing temperature as a function of radius (Lee et al. 2017; Villenave et al. 2020; Ohashi et al. 2022; Takakuwa et al. prep). We also demonstrate the feasibility through modeling in Section 4. In addition, the optically thinner $\lambda = 2.1$ mm (ALMA Band 4) image with similar resolution ($\sim 0.06''$; 10 au) does not show a similar asymmetry (Villenave et al. 2020) which should be expected if the disk is intrinsically asymmetric.

By assuming the emission at $\nu = 225$ GHz comes entirely from the dust thermal emission and is optically thin, one can estimate the total dust mass disk through

$$M_{\rm dust} = \frac{D^2 S_\nu}{\kappa_\nu B_\nu(T)} \tag{2}$$

where $S_\nu = \int I_\nu d\Omega$ is the flux density, κ_ν is the mass opacity in cm^2 g^{-1} of dust, D is the distance to the source, T is the temperature in Kelvin, and B_ν is the black body radiation using the Planck function. We adopt the opacity of 0.023 cm^2 g^{-1} of gas from Beckwith et al. (1990) (see also recent evidence from Lin et al. 2021 in support of this prescription and Section 4) and assume a dust-to-gas mass ratio of 0.01 to obtain $\kappa_\nu = 2.3$ cm^2 g^{-1} of dust. We assume $T = 20$ K which is a commonly adopted value for surveys (e.g. Andrews & Williams 2005; Ansdell et al. 2016; Tobin et al. 2020). Since $D = 160$ pc and $S_\nu = 184$ mJy for IRAS 04302, we have $M_{\rm dust} \sim 140 M_\oplus$. Another way to estimate a representative temperature is based on the bolometric luminosity

$$T = 43(L_{\rm bol}/L_\odot)^{1/4} \tag{3}$$

which is optimized at a radius of 50 au (Tobin et al. 2020). With $L_{\rm bol} = 0.43 L_\odot$ (Ohashi et al. prep), we have $T \sim 34$ K and the dust mass is $M_{\rm dust} \sim 70 M_\oplus$. Note that since the disk is clearly not optically thin (as we can see from the asymmetry from the minor axis due to optical depth effects) the estimate here is a lower limit and likely a drastic underestimation given the near edge-on view.

4 CONTINUUM FORWARD RAY TRACING

Although a 2D Gaussian captures the overall features, such as the position angle and the overall shape, certain deviations stand out. Fig. 3a shows the original continuum and the fitted 2D Gaussian, while Fig. 3b shows the residuals, which are defined as the observed image subtracted by the 2D Gaussian. The largest deviation is the significant positive residual extending parallel to the disk major axis that is slightly offset from the center to the east. This corresponds to the asymmetry along the minor axis where the east side is brighter.

In this section, we demonstrate that the asymmetry along the minor axis is due to the inclination effect of an optically thick disk. We use a parameterized disk model and use RADMC-3D[1] to conduct the ray-tracing (Dullemond et al. 2012). We refrain from conducting the heating/cooling calculations from RADMC-3D given the large computational cost and complexities regarding the dust opacity spectrum (e.g. Birnstiel et al. 2018). The calculation is beyond the scope of this paper and we leave it to a future paper (Takakuwa et al. prep).

The parameterized disk model is a similar version of the disk model from Lin et al. (2021) which is suited for a disk viewed near edge-on. The model was applied to a Class 0 edge-on source, HH 212 mms, and successfully reproduced the asymmetry along the minor

[1] RADMC-3D is available at `https://www.ita.uni-heidelberg.de/~dullemond/software/radmc-3d/`.

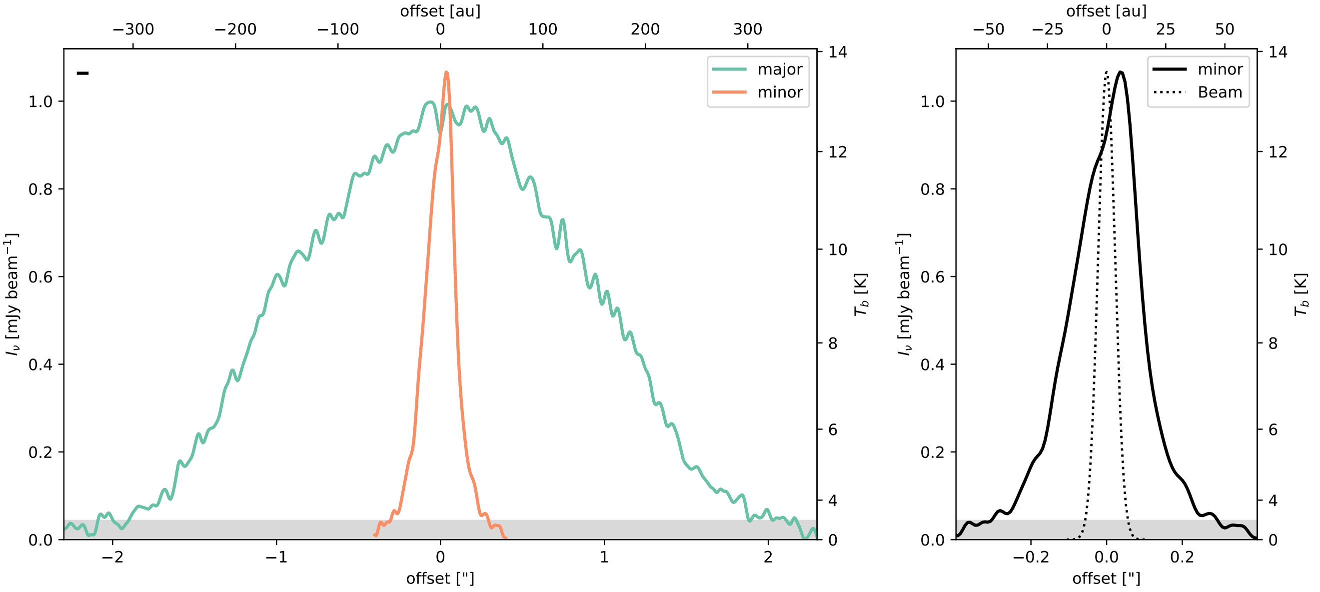

Figure 2. Left panel: The cuts along the major and minor axis of the continuum disk by interpolating the image. The cut along the major axis is in green and that along the minor axis is in orange. The origin is at the center of the fitted 2D Gaussian (04:33:16.5, +22:53:20.2). The bottom and top axes mark the offset from the origin along the cut in arcsec and au. The positive location for the major axis is along the northern part of the disk, while the positive location for the minor axis is along the eastern part of the disk. The left and right axes mark the intensity in mJy beam^{-1} and brightness temperature (using the full Planck function) in Kelvin respectively. The line segment to the upper left corner represents the length of the FWHM of the beam. The shaded region is the intensity below 3σ. Right panel: Zoom-in comparison between the minor axis cut (solid black line) and the beam (dotted black line).

axis across ALMA Bands 3, 6, and 7. In the following, we briefly describe the key parts of the model and include modifications.

We parameterize the disk using the Toomre Q parameter (Toomre 1964)

$$Q \equiv \frac{c_s \Omega_k}{\pi G \Sigma} \tag{4}$$

where c_s is the isothermal velocity, $\Omega_k \equiv \sqrt{GM_*/R^3}$ is the Keplerian frequency, R is the cylindrical radius, and Σ is the gas surface density. For a gravitationally stable disk, Q must be greater than a value of order unity (e.g. Kratter & Lodato 2016). The pressure scale height of the gas is

$$H_g \equiv \frac{c_s}{\Omega_k} . \tag{5}$$

From basic arguments of vertical hydrostatic equilibrium, the gas density in the midplane is $\rho_{g,\mathrm{mid}} = \Sigma/\sqrt{2\pi}/H_g$ and thus, when combined with Eq. (4), we have

$$\rho_{g,\mathrm{mid}}(R) = \frac{M_*}{\pi\sqrt{2\pi}R_0^3 Q}\left(\frac{R}{R_0}\right)^{-3}, \tag{6}$$

where R_0 is a characteristic radius, which we take to be the outer radius of the disk. For illustrative purposes, we assume that Q is a constant in the disk, and introduce a characteristic density $\rho_0 \equiv M_*/(\pi\sqrt{2\pi}R_0^3 Q)$, which is the density at the disk outer edge.

Since the dust disk appears vertically thin, we approximate the temperature with just a vertically isothermal prescription:

$$T(R) = T_0\left(\frac{R}{R_0}\right)^{-q} \tag{7}$$

where T_0 is the temperature at the outer edge of the disk and q specifies the temperature gradient. Note that the whole gas disk should have a vertical temperature gradient (warmer temperature in the atmosphere), which is needed for the existence of the clear snow surface (Lin et al. prep). However, since the bulk of the dust disk appears to lie below the snow surface and there is no continuum dark lane (such as that found for HH 212 mms), the effect of a vertical temperature gradient is likely marginal and thus, we only use a vertically isothermal profile for the dust disk.

As a further simplification, we fix $q = 0.5$ which is expected from passively irradiated disks in radiative equilibrium (e.g. Chiang & Goldreich 1997; D'Alessio et al. 1998). This assumption may not be entirely applicable to embedded protostars, which can have additional accretion heating or warming from the envelope (e.g. Butner et al. 1994; Agurto-Gangas et al. 2019). Accretion heating should lead to a steeper temperature gradient, usually $q = 0.75$ (Armitage 2015), and dominate the inner regions of the disk (Takakuwa et al. prep). Envelope warming prevails in the outer regions and should make the temperature gradient shallow (e.g., $q \leq 0.4$ from Whitney et al. 2003). The Class I designation of IRAS 04302 motivates a smaller q, however, van't Hoff et al. (2020) found $q = 0.75$ based on the location of snow lines of H_2CO and $C^{17}O$ though the resolution is not ideal. We also refrain from fitting q directly, since a single wavelength image of an edge-on disk probes a limited range in radius due to the high optical depth (Lin et al. 2021). Longer wavelength observations are necessary to probe the temperature of the inner regions and using multiwavelength observations that probe different radii will better constrain q. Thus, given the uncertainties, we fix $q = 0.5$ as a compromise for this paper and leave the exploration of q for a future study.

Lin et al. (2021) assumed that the dust and the gas are well-coupled and thus the dust also follows the gas in hydrostatic equilibrium (qualitatively, this means the dust scale height is equal to the gas scale height if the disk is vertically isothermal). However, to directly

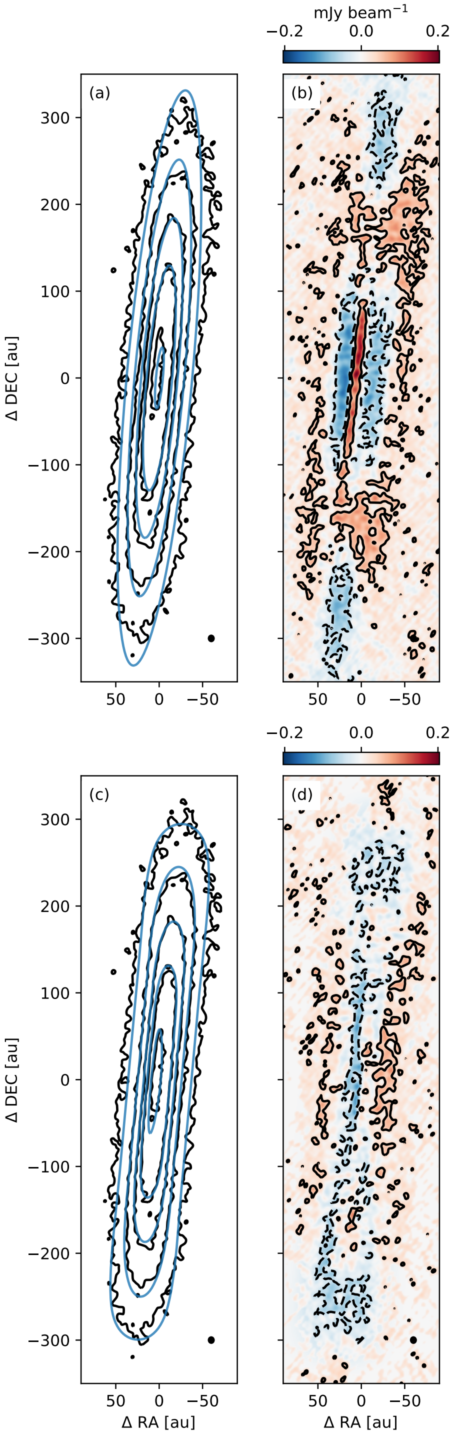

Figure 3. Comparisons between the observed continuum and models. The top row shows the 2D Gaussian model, while the bottom row shows the model with radiative transfer (see Section 4). The plots in the left column show the model (in blue contours) plotted against the observed continuum (in black contours). The color maps in the right column shows the residuals (the observed subtracted by the model) in mJy beam^{-1}. The solid and dashed contours trace the 3σ and -3σ levels respectively.

Parameter	Variable	Value
Inclination	i	87°
Disk Edge	R_0	310 au
Temperature at R_0	T_0	7.5 K
Dust Scale Height at 100 au	H_{100}	6 au
Characteristic Optical Depth	$\tau_{0,\nu}$	0.35
RA offset of star	$\delta_{\rm RA}$	-0.03″
DEC offset of star	$\delta_{\rm DEC}$	-0.04″

Table 1. Adopted parameters for the dust model . These are the parameters from the search by hand that appear to match best and provide the model in Fig. 3. The RA and DEC offset are relative to the center based on the 2D Gaussian fitting in Section 3.

explore the dust scale height independent of what the gas scale height should be, we parameterize the dust scale height by

$$H_d(R) = H_{100}\left(\frac{R}{100\text{ au}}\right)^{1.25} \tag{8}$$

where the power-law index is the same as that from the gas scale height, i.e., $1.5 - q/2$. Eq. (8) allows us to easily explore the effects of height with one parameter H_{100}.

By assuming that the midplane density of the dust is related to the midplane density of the gas (Eq. (6)) through a dust-to-gas mass ratio η, the complete dust density as a function of radius and height is

$$\rho_d(R,z) = \rho_{d,0}\left(\frac{R}{R_0}\right)^{-3} \exp\left[-\frac{1}{2}\left(\frac{z}{H_d}\right)^2\right] \tag{9}$$

where z is the vertical height and $\rho_{d,0} \equiv \rho_0/\eta$ is the midplane dust density at the outer edge of the disk.

Instead of prescribing the dust opacity κ_ν (in units of cm^2 per gram of dust) explicitly, we use the characteristic optical depth $\tau_{0,\nu}$ defined as

$$\tau_{0,\nu} \equiv \rho_{d,0} R_0 \kappa_\nu. \tag{10}$$

The definition makes sense because the characteristic length scale along the line of sight for an edge-on disk is R_0. This parameter reflects the fact that opacity and density are degenerate and it is the optical depth (proportional to the product of opacity and density) that controls how an image appears (see Lin et al. 2021 for detailed derivation and for exploration of how $\tau_{0,\nu}$ controls the image of an edge-on disk). In other words, $\tau_{0,\nu}$ is a free parameter that we can fit from the image.

As an initial exploration for this paper, we conduct the parameter search by hand. To limit the parameter space, we fix the position angle to 174.77° obtained from the 2D Gaussian fit. The free parameters include $\tau_{0,\nu}$, T_0, i, R_0 and H_{100} in addition to the location of the star ($\delta_{\rm RA}$, $\delta_{\rm DEC}$). The parameters for the best fit model are listed in Table 1.

Fig. 3c shows that the model compares quite well with the observations. The dust model can easily reproduce the shift along the minor axis towards the far side of the disk (towards the east for the case of IRAS 04302), since the disk is optically thick and highly inclined (Villenave et al. 2020; Takakuwa et al. prep). The residuals are shown in Fig. 3d and are evidently much lower than that from the simple 2D Gaussian fit (Fig. 3b).

We find that the H_{100} is 6 au. The dust scale height from past modeling efforts based on lower resolution mm-images varies in the literature and ranges from ∼ 2 au to 15 au at a radius of 100 au (Wolf et al. 2003, 2008; Gräfe et al. 2013; Sheehan & Eisner 2017) though it depends on the exact prescription of each model. By resolving the asymmetry along the minor axis, the new high-resolution image presented here offers a strong constraint on the dust scale height. In addition, the value is consistent with an independent study which modeled another high-resolution image at Band 4 (Villenave et al., in prep.; private communication). On the other hand, the derived radius of $R_0 = 310$ au is consistent with past modeling efforts based on lower resolution mm-images in which case the major axis of the disk was well resolved (Wolf et al. 2003; Gräfe et al. 2013).

The inferred inclination of $i = 87^\circ$ provides the necessary deviation from being perfectly edge-on ($i = 90^\circ$) which would not produce an asymmetry along the minor axis since both halves across the midplane would be perfectly symmetric (e.g. Wolf et al. 2003). The value is also consistent with the lower limit of $\sim 84^\circ$ assuming the disk is completely flat (see Section 3). It is not surprising that the actual inclination is larger than the inclination inferred just from the ratio between the minor and major axes, or arccos(minor/major). Using the ratio assumes that only the radial extent contributes to the projected length along the minor axis which is indeed the case for a geometrically thin disk. However, for a highly inclined geometrically thick disk, the vertical thickness contributes to the projected width along the minor axis which decreases arccos(minor/major).

The inferred T_0 of 7.5 K appears to be lower than necessary when compared to what is expected from the estimated snow line of CO. The low temperature profile is necessary, because the peak brightness temperature is only ~ 14 K and yet the disk has to be optically thick to produce the minor axis shift of the continuum. Based on the fitted T_0, the snow line for CO, assuming a freeze out temperature of 20 K, should be at ~ 44 au ($0.275''$). However, this appears inconsistent with the observed location of the snow line which is ~ 130 au ($\sim 0.8''$) from $C^{18}O$ (also similar to what was derived in van 't Hoff et al. 2018 from lower angular resolution observations of $C^{17}O$). One possibility is that the dust temperature profile is correct and the observed $C^{18}O$ emission beyond the inferred snow line location (of 44 au) is contaminated by emission from the warmer surface layers due to the finite beam.

Another possibility to alleviate the above discrepancy is through scattering. Scattering makes objects appear dimmer, which means the actual temperature should be higher than what is inferred when assuming no scattering (e.g. Birnstiel et al. 2018). Interestingly, radiation transfer calculations for this source including scattering of 100 μm grains infer a temperature of 20 K at 100 au (Gräfe et al. 2013) which is higher than the 13 K at 100 au based on the model prescribed here. Given that scattering only scales the image intensities and does not alter the relative shape of the image much (Lin et al. 2021), the inferred low temperature could be evidence of scattering, but we leave the incorporation of scattering to a future study.

Intriguingly, the outermost contour of the model appears systematically less extended than the observations along the minor axis (Fig. 3c). This is also seen as two lanes of generally positive residuals to the east and west of the disk in Fig. 3d which suggests a more extended upper layer. However, increasing H_c to broaden the image along the minor axis leads to even broader widths at the end points of the major axis of the disk. Thus, it appears that the dust scale height should not be too flared at outer radius compared to the inner radius. This is in fact what we would expect from dust settling of a given grain size, where the outer region should be more settled than the inner region, because the Stokes number of the grains increase as the density decreases towards larger radii (Dullemond & Dominik 2004). We leave also this possibility for a future exploration.

We found that the characteristic optical depth is $\tau_{0,\nu} = 0.35$ which can be related to the opacity. From Eq. (10) and the definition of ρ_0 from Eq. (6), we can explicitly solve for κ_ν through

$$\kappa_\nu = \frac{\pi\sqrt{2\pi}Q\eta\tau_0 R_0^2}{M_*}. \tag{11}$$

Using the best fit R_0 and $\tau_{0,\nu}$ from this section, the M_* derived based on the rotation curve of $C^{18}O$ (see Section **??**), the opacity is $\kappa_\nu = 0.019Q\eta$ in units of cm^2 g^{-1} of gas. If the disk is gravitationally stable, Q should be greater than of order unity. Otherwise, the disk should fragment (Kratter & Lodato 2016). Thus, taking $Q = 1$ gives a lower limit to κ_ν. We note that the lower limit to the opacity is per mass of gas, since it is the gas that contributes most of the mass and that limits the amount material. However, theoretical dust models calculate dust opacity with respect to the mass of the dust (e.g. Ossenkopf & Henning 1994) and thus we have to assume a η to directly compare the dust opacity calculations to the observationally constrained opacity presented here. By assuming the standard $\eta = 100$, we get $\kappa_\nu = 1.9Q$ cm^2 g^{-1} of dust. The uncertainty of κ_ν is 0.5 cm^2 g^{-1} of dust based on error propagation from the uncertainty of M_* derived in Section **??**. We add the caveat that the opacity can vary spatially which is not captured through the model and thus, the value measured here is an effective opacity of the region observable at Band 6.

The conventional Beckwith et al. (1990) opacity at λ=1.3 mm is $\kappa_\nu = 2.3$ cm^2 g^{-1} of dust (also constrained observationally and assumed $\eta = 100$) and the opacity based on HH 212 mms is $\kappa_\nu = 1.33$ cm^2 g^{-1} of dust (Lin et al. 2021). By taking $Q = 1$, it appears that the lower limit from IRAS 04302 lies right in between the two previous studies as shown in Fig. 4. For completeness, we have included opacity constraints at other wavelengths for HH 212 mms (Lin et al. 2021) and also another commonly adopted dust opacity model from Ossenkopf & Henning (1994) with calculations adopted for low and high densities. The lower limit from IRAS 04302 disfavors the opacity model from Ossenkopf & Henning (1994) and is more consistent with the Beckwith et al. (1990) prescription.

The proximity of the lower limit from IRAS 04302 to the opacity from HH 212 mms is intriguing, given that HH 212 mms is vastly different compared to IRAS 04302 in class, size of the disk, and stellar mass. While HH 212 mms is likely to be marginally gravitationally unstable given the small stellar mass, bright continuum, and early stage (Tobin et al. 2020), IRAS 04302, as a Class I source, is less certain. Even if grains have a universal opacity, the lower limit from IRAS 04302 need not be similar, since from Eq. (11), taking $Q = 1$ is only a lower limit after all and Q can take on any value greater than 1 if the disk is not marginally gravitationally unstable.

If not purely coincidental, a possible physical explanation is that the grains could be similar between these two systems *and* both systems are marginally gravitationally unstable which fixes Q to a value of order unity (e.g. Lodato 2007; Kratter & Lodato 2016; Xu & Kunz 2021). It may not be too surprising if IRAS 04302 can also be marginally gravitationally unstable given the large disk, available reservoir of envelop material, and cold midplane temperature. There is growing evidence of other Class 0/I sources that are marginally graviationally unstable (Tobin et al. 2020; Xu 2022). Furthermore, from an evolutionary standpoint, this is in line with evidence of Class II sources with Q that largely falls within 1 to 10 (e.g. Cleeves et al. 2016; Booth et al. 2019; Veronesi et al. 2021; Paneque-Carreño et al. 2021; Ueda et al. 2022; Schwarz et al. 2021; Sierra et al. 2021; Yoshida et al. 2022; Lodato et al. 2022).

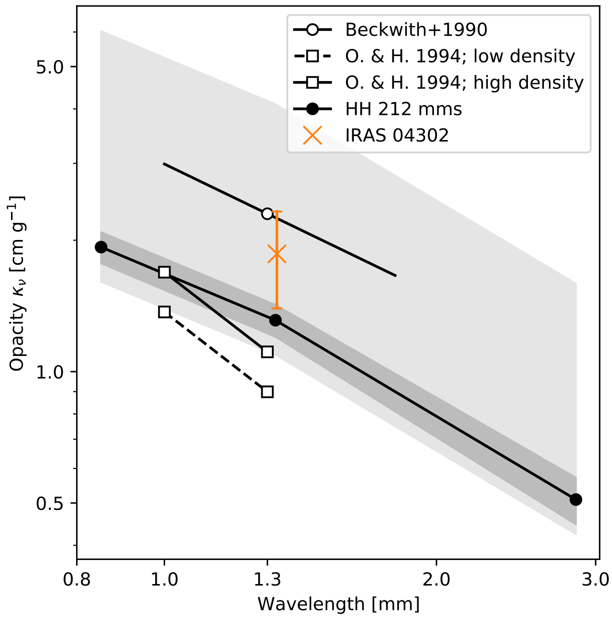

Figure 4. The lower limit to the dust opacity (absorption cross section per gram of dust assuming a dust-to-gas ratio of 0.01) inferred from the IRAS 04302 disk (marked as an orange cross) in comparison to other millimeter dust opacities from the literature. The error bar is the uncertainty associated with the uncertainty from the stellar mass. The filled circles with solid lines are the lower limit to the dust opacity for the HH 212 mms disk from Lin et al. (2021). The corresponding lighter shaded region is the uncertainty associated with the stellar mass and also the Toomre Q parameter (ranging 1 to 2.5) and the darker shaded region is the uncertainty from the noise. The open circle is the Beckwith et al. (1990) opacity at 1.3 mm and its line segment represents the opacity index of 1. The open squares are opacities from Ossenkopf & Henning (1994) at 1 and 1.3 mm.

5 DISCUSSION

One of the most striking features of the IRAS 04302 disk is the shift of the intensity peak along the minor axis of the continuum image which is a tell-tale sign of dust with finite vertical extent, i.e., non-settled dust. This feature exists for several other sources among the eDisk sample, including CB 68 (Kido et al. prep), L1527 IRS (van't Hoff et al. prep), IRS 7B (Ohashi et al. prep; Takakuwa et al. prep), GSS 30 IRS3 (Santamaría-Miranda et al. prep), IRAS 32 (Encalada et al. prep), BHR 71 (Gavino et al. prep), IRAS 04169+2702 (Han et al. prep), and IRAS 16253-2429 (Aso et al. prep).

In one extreme, dust settled into an infinitely thin sheet should appear symmetric across the minor axis and for disks with rings, the rings and gaps should not show azimuthal variation (e.g. Pinte et al. 2016; Doi & Kataoka 2021). Several observations of Class II sources show that the dust is predominantly well settled (e.g. Andrews et al. 2018; Long et al. 2018; Villenave et al. 2020; Doi & Kataoka 2021; Liu et al. 2022; Villenave et al. 2023). One of the clearest case is SSTC2D J163131.2-242627 (or Oph 163131 for short) whose gaps are resolved even though the disk is near edge-on (Villenave et al. 2022, $i \sim 84°$). The inferred dust scale height is ≤ 0.5 au at 100 au, which is an order of magnitude smaller than that of IRAS 04302. Furthermore, the significant difference in the vertical extent of the gas and dust also shows that dust is decoupled from the gas over most of the disk volume away from the midplane (e.g. Villenave et al. 2020; Law et al. 2021, 2022).

In the other extreme, the Class 0 source, HH 212 mms, hosts a clear dark lane sandwiched between two bright lanes in the dust continuum at $\sim$ 1 mm, which is evidence that the dust is elevated high enough to trace the warm surface layers. The dust scale height is $\sim$ 12 au at a radius of $\sim$ 36 au and the dust was shown to follow the gas in hydrostatic equilibrium (Lee et al. 2017; Lin et al. 2021).

From Section 4, we found that the dust scale height is 6 au at a radius of 100 au. For comparison, the gas pressure scale height from Eq. (5) is $H_g = 5.8 \pm 0.7$ au at a radius of 100 au after adopting $M_* = 1.6 \pm 0.4 M_\odot$ from Lin et al. (prep) and the dust isothermal temperature profile of Eq. (7) with the best fit T_0 (only the stellar mass uncertainty is included here). The effectively equivalent scale heights given the uncertainties suggest that the dust has not separated from the gas vertically.

We caution that there is ambiguity in the midplane temperature, since the temperature derived from dust modeling appears different from the temperature inferred from the freeze-out location of CO. Using the snow line of 130 au (Lin et al. prep) and assuming a freeze-out temperature of 20 K with $q = 0.5$, the temperature at 100 au is $\sim$ 23 K and results in $H_g = 7.6 \pm 1.0$ au. Considering the ambiguity of the temperature profile from the two scenarios, we have $\sim 0.8 \leq H_d/H_g \leq\sim 1$. We also note that H_d inferred from Section 4 assumes a mixed, single population of grains. However, if grain growth has occurred, we may expect grains of different sizes to settle at various characteristic heights (e.g. Dubrulle et al. 1995). Nevertheless, the inferred H_d represents the characteristic height of the bulk of the material that is responsible for the $\lambda = 1.3$ mm emission which is already different from the Class II sources that are settled as mentioned above. At face-value, the non-significant level of dust settling may pose difficulties for the streaming instability to produce planetesimals (Gole et al. 2020).

Although the dust traced by 1.3 mm continuum is non-settled, the dust in general appears very distinct from the distribution of gas molecules (Lin et al. prep) and also very distinct from the scattered light images of IRAS 04302. Fig. 5 shows a comparison between the 1.3 mm continuum, ^{13}CO, and scattered light images from the Hubble Space Telescope (HST) at 1.6 μm (Padgett et al. 1999). We describe the correction for proper motion in Lin et al. (prep). Strikingly, each image traces a spatially distinct location. The 1.3 mm continuum appears only near the midplane, while the scattered light only exists in the bipolar cavities. ^{13}CO fills the atmospheric regions of the disk and reaches beyond the radial extent of the 1.3 mm continuum and scattered light. Nevertheless, the gas pressure scale height H_g of 6 $\sim$ 7 au may not be too surprising, since the line emission can typically be at several pressure scale heights above the midplane (e.g. Dullemond & Dominik 2004; Wolff et al. 2021; Flores et al. 2021; Villenave et al. 2022; Law et al. 2022; Paneque-Carreño et al. 2022), and small dust grains are present in the bipolar nebula to scatter optical/IR light. Detailed modeling using the high-angular resolution observations of the molecular lines with the dust could give a more robust view on the level of dust settling.

Another distinction between the gas and mm-continuum is the radial extent. The edge of the dust disk has a radius of $\sim$ 310 au (see Section 4), while the edge of the gas disk has a radius of $\sim$ 620 au (Lin et al. prep). In light of the disparity in the dust and gas radii, but similarity in the dust and gas scale heights (see Section 4), IRAS 04302 demonstrates that radial settling occurs sooner than vertical settling. Nevertheless, proper forward ray tracing including both the dust and gas will make the disparity more definitive.

IRAS 04302 is formally a Class I source based on the SED (Ohashi et al. prep). Although an object with the Class I designation could actually be a Class II source if viewed edge-on, there is additional

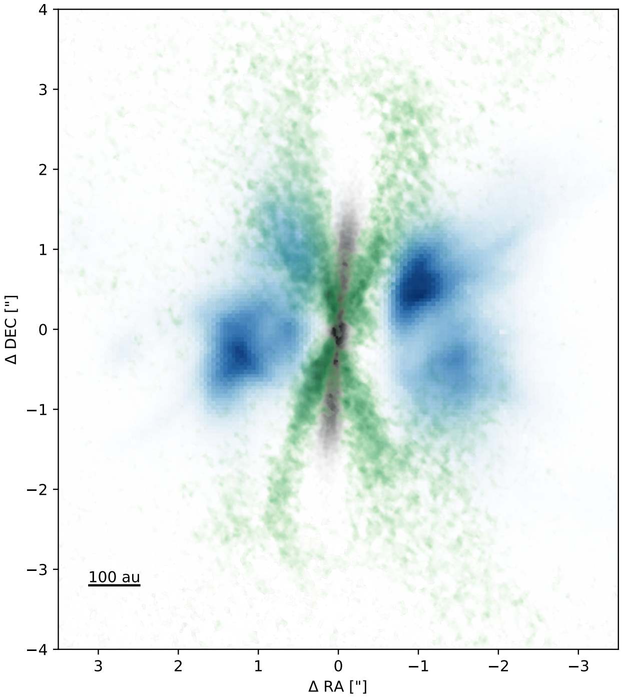

Figure 5. Composite image comparing the 1.3 mm continuum (black), 1.6 μm from the HST (blue), and ^{13}CO with robust=0.5 (green).

evidence that IRAS 04302 is indeed younger than formal Class II sources. First, the scattered light image of IRAS 04302 is noticeably irregular which indicates potential interactions with its envelope. In contrast, scattered light images of Class II sources tend to be well-ordered (Villenave et al. 2020). Second, IRAS 04302 has clear evidence of extended ^{13}CO and ^{12}CO emission beyond the Keplerian disk surface with kinematics inconsistent with Keplerian rotation which is likely part of the envelope (Lin et al. prep). Thus, it is quite clear that this Class I source is a case where there is relatively little dust settling amid infall and outflow. Given that most Class II sources appear settled, we speculate that substantial dust settling should happen between the Class I stage and Class II stage.

It is curious whether IRAS 04302 has any radial substructure given its Class I stage. Rings and gaps are ubiquitous around Class II protostars (e.g Andrews et al. 2018; Long et al. 2018) and these structures could be signposts of planets (e.g. Zhang et al. 2018). Gaps from a highly inclined disk like Oph 163131 were resolved (Villenave et al. 2022), but the order of magnitude larger dust scale height of IRAS 04302 can easily obscure the gaps if there exists any.

6 CONCLUSION

As part of the ALMA large program, eDisk, we presented high resolution ALMA Band 6 dust continuum and line emission of the nearly edge-on Class I disk IRAS 04302. Our main results are as follows:

(i) The dust continuum image has an angular resolution of $\sim 0.05''$ ($\sim$ 8 au) and shows a nearly edge-on disk with a clear brightness asymmetry along the disk minor axis. By fitting the disk with a 2D Gaussian, we find that the lower limit to the inclination is $\sim 83.6°$ using the ratio of the major and minor axis FWHM. Through forward ray tracing of the dust, we find that the inclination is $\sim 87°$ and that the disk needs to be optically thick and geometrically thick to produce minor axis asymmetry. There is no evidence of rings and gaps, which could be due to the lack of radial substructure or because the highly inclined and optically thick view obscures the gaps.

(ii) Our most important conclusion is that the dust has yet to settle significantly in the Class I IRAS 04302 disk. We find a dust scale height $\sim$ 6 au at a radius of 100 au, which is comparable to the gas scale at the same radius. This result, coupled with the lack of dust settling in Class 0 disks, such as HH 212 mms, indicates that substantial dust settling should happen between the Class I stage and Class II stage.

ACKNOWLEDGEMENTS

ZYDL acknowledges support from the Virginia Space Grant Consortium (VSGC), NASA 80NSSC18K1095, the Jefferson Scholars Foundation, the NRAO ALMA Student Observing Support (SOS) SOSPA8-003, the Achievements Rewards for College Scientists (ARCS) Foundation Washington Chapter, and UVA research computing (RIVANNA). This paper makes use of the following ALMA data: ADS/JAO.ALMA#2019.1.00261.L. ALMA is a partnership of ESO (representing its member states), NSF (USA) and NINS (Japan), together with NRC (Canada), MOST and ASIAA (Taiwan), and KASI (Republic of Korea), in cooperation with the Republic of Chile. The Joint ALMA Observatory is operated by ESO, AUI/NRAO and NAOJ. The National Radio Astronomy Observatory is a facility of the National Science Foundation operated under cooperative agreement by Associated Universities, Inc.

REFERENCES

Agurto-Gangas C., et al., 2019, A&A, 623, A147
Aikawa Y., van Zadelhoff G. J., van Dishoeck E. F., Herbst E., 2002, A&A, 386, 622
Akimkin V., Zhukovska S., Wiebe D., Semenov D., Pavlyuchenkov Y., Vasyunin A., Birnstiel T., Henning T., 2013, ApJ, 766, 8
Andrews S. M., Williams J. P., 2005, ApJ, 631, 1134
Andrews S. M., et al., 2018, ApJ, 869, L41
Ansdell M., et al., 2016, ApJ, 828, 46
Armitage P. J., 2015, arXiv e-prints, p. arXiv:1509.06382
Aso Y., Ohashi N., Jørgensen J. K., Tobin J. J., in prep., ApJ
Beckwith S. V. W., Sargent A. I., Chini R. S., Guesten R., 1990, AJ, 99, 924
Birnstiel T., et al., 2018, ApJ, 869, L45
Booth A. S., Walsh C., Ilee J. D., Notsu S., Qi C., Nomura H., Akiyama E., 2019, ApJ, 882, L31
Briggs D. S., 1995, PhD thesis, New Mexico Institute of Mining and Technology
Butner H. M., Natta A., Evans Neal J. I., 1994, ApJ, 420, 326
Chiang E. I., Goldreich P., 1997, ApJ, 490, 368
Cleeves L. I., Öberg K. I., Wilner D. J., Huang J., Loomis R. A., Andrews S. M., Czekala I., 2016, ApJ, 832, 110
Czekala I., et al., 2021, ApJS, 257, 2
D'Alessio P., Cantö J., Calvet N., Lizano S., 1998, ApJ, 500, 411
Doi K., Kataoka A., 2021, ApJ, 912, 164
Drazkowska J., et al., 2022, arXiv e-prints, p. arXiv:2203.09759
Dubrulle B., Morfill G., Sterzik M., 1995, Icarus, 114, 237
Dullemond C. P., Dominik C., 2004, A&A, 421, 1075
Dullemond C. P., Juhasz A., Pohl A., Sereshti F., Shetty R., Peters T., Commercon B., Flock M., 2012, RADMC-3D: A multi-purpose radiative transfer tool, Astrophysics Source Code Library, record ascl:1202.015 (ascl:1202.015)

Dutrey A., et al., 2014, in Beuther H., Klessen R. S., Dullemond C. P., Henning T., eds, Protostars and Planets VI. pp 317–338 (arXiv:1402.3503), doi:10.2458/azu_uapress_9780816531240-ch014
Eisner J. A., 2012, ApJ, 755, 23
Encalada F., Ohashi N., Jørgensen J. K., Tobin J. J., in prep., ApJ
Flores C., et al., 2021, AJ, 161, 239
Furlan E., et al., 2008, ApJS, 176, 184
Galli P. A. B., et al., 2018, ApJ, 859, 33
Gavino S., Ohashi N., Jørgensen J. K., Tobin J. J., in prep., ApJ
Gole D. A., Simon J. B., Li R., Youdin A. N., Armitage P. J., 2020, ApJ, 904, 132
Gräfe C., Wolf S., Guilloteau S., Dutrey A., Stapelfeldt K. R., Pontoppidan K. M., Sauter J., 2013, A&A, 553, A69
Han I., Ohashi N., Jørgensen J. K., Tobin J. J., in prep., ApJ
Kenyon S. J., Dobrzycka D., Hartmann L., 1994, AJ, 108, 1872
Kido M., Ohashi N., Jørgensen J. K., Tobin J. J., in prep., ApJ
Kratter K., Lodato G., 2016, ARA&A, 54, 271
Law C. J., et al., 2021, ApJS, 257, 4
Law C. J., et al., 2022, ApJ, 932, 114
Lee C.-F., Li Z.-Y., Ho P. T. P., Hirano N., Zhang Q., Shang H., 2017, Science Advances, 3, e1602935
Lee C.-F., Li Z.-Y., Turner N. J., 2020, Nature Astronomy, 4, 142
Lesur G., et al., 2022, arXiv e-prints, p. arXiv:2203.09821
Li Z. Y., Banerjee R., Pudritz R. E., Jørgensen J. K., Shang H., Krasnopolsky R., Maury A., 2014, in Beuther H., Klessen R. S., Dullemond C. P., Henning T., eds, Protostars and Planets VI. p. 173 (arXiv:1401.2219), doi:10.2458/azu_uapress_9780816531240-ch008
Lin Z.-Y. D., Lee C.-F., Li Z.-Y., Tobin J. J., Turner N. J., 2021, MNRAS, 501, 1316
Lin Z.-Y. D., Li Z.-Y., Tobin J. J., Jørgensen J. K., in prep., ApJ
Liu Y., et al., 2022, Science China Physics, Mechanics, and Astronomy, 65, 129511
Lodato G., 2007, Nuovo Cimento Rivista Serie, 30, 293
Lodato G., et al., 2022, arXiv e-prints, p. arXiv:2211.03712
Long F., et al., 2018, ApJ, 869, 17
Lucas P. W., Roche P. F., 1997, MNRAS, 286, 895
Lucas P. W., Roche P. F., 1998, MNRAS, 299, 723
Luhman K. L., 2018, AJ, 156, 271
McMullin J. P., Waters B., Schiebel D., Young W., Golap K., 2007, in Shaw R. A., Hill F., Bell D. J., eds, Astronomical Society of the Pacific Conference Series Vol. 376, Astronomical Data Analysis Software and Systems XVI. p. 127
Michel A., Sadavoy S. I., Sheehan P. D., Looney L. W., Cox E. G., 2022, ApJ, 937, 104
Nakagawa Y., Sekiya M., Hayashi C., 1986, Icarus, 67, 375
Ohashi S., Kataoka A., 2019, ApJ, 886, 103
Ohashi S., Nakatani R., Liu H. B., Kobayashi H., Zhang Y., Hanawa T., Sakai N., 2022, ApJ, 934, 163
Ohashi N., Jørgensen J. K., Tobin J. J., in prep., ApJ
Ossenkopf V., Henning T., 1994, A&A, 291, 943
Padgett D. L., Brandner W., Stapelfeldt K. R., Strom S. E., Terebey S., Koerner D., 1999, AJ, 117, 1490
Paneque-Carreño T., et al., 2021, ApJ, 914, 88
Paneque-Carreño T., Miotello A., van Dishoeck E. F., Tabone B., Izquierdo A. F., Facchini S., 2022, arXiv e-prints, p. arXiv:2210.01130
Pinte C., Dent W. R. F., Ménard F., Hales A., Hill T., Cortes P., de Gregorio-Monsalvo I., 2016, ApJ, 816, 25
Podio L., et al., 2020, A&A, 642, L7
Roccatagliata V., Franciosini E., Sacco G. G., Randich S., Sicilia-Aguilar A., 2020, A&A, 638, A85
Sakai N., et al., 2017, MNRAS, 467, L76
Santamaría-Miranda A., Ohashi N., Jørgensen J. K., Tobin J. J., in prep., ApJ
Schwarz K. R., et al., 2021, ApJS, 257, 20
Sheehan P. D., Eisner J. A., 2017, ApJ, 851, 45
Sierra A., et al., 2021, ApJS, 257, 14
Takakuwa S., Ohashi N., Jørgensen J. K., Tobin J. J., in prep., ApJ
Terebey S., Shu F. H., Cassen P., 1984, ApJ, 286, 529
Testi L., et al., 2014, in Beuther H., Klessen R. S., Dullemond C. P., Henning T., eds, Protostars and Planets VI. p. 339 (arXiv:1402.1354), doi:10.2458/azu_uapress_9780816531240-ch015
Tobin J. J., Hartmann L., Loinard L., 2010, ApJ, 722, L12
Tobin J. J., et al., 2020, ApJ, 890, 130
Toomre A., 1964, ApJ, 139, 1217
Tsukamoto Y., et al., 2022, arXiv e-prints, p. arXiv:2209.13765
Tu Y., Li Z.-Y., Lam K. H., 2022, MNRAS, 515, 4780
Ueda T., Kataoka A., Tsukagoshi T., 2022, ApJ, 930, 56
Veronesi B., Paneque-Carreño T., Lodato G., Testi L., Pérez L. M., Bertin G., Hall C., 2021, ApJ, 914, L27
Villenave M., et al., 2020, A&A, 642, A164
Villenave M., et al., 2022, ApJ, 930, 11
Villenave M., et al., 2023, arXiv e-prints, p. arXiv:2302.01949
Weidenschilling S. J., 1977, MNRAS, 180, 57
Whitney B. A., Wood K., Bjorkman J. E., Wolff M. J., 2003, ApJ, 591, 1049
Wolf S., Padgett D. L., Stapelfeldt K. R., 2003, ApJ, 588, 373
Wolf S., Schegerer A., Beuther H., Padgett D. L., Stapelfeldt K. R., 2008, ApJ, 674, L101
Wolff S. G., et al., 2021, AJ, 161, 238
Xu W., 2022, ApJ, 934, 156
Xu W., Kunz M. W., 2021, MNRAS, 502, 4911
Yoshida T. C., Nomura H., Tsukagoshi T., Furuya K., Ueda T., 2022, ApJ, 937, L14
Youdin A. N., Goodman J., 2005, ApJ, 620, 459
Zhang S., et al., 2018, ApJ, 869, L47
van 't Hoff M. L. R., Tobin J. J., Harsono D., van Dishoeck E. F., 2018, A&A, 615, A83
van't Hoff M. L. R., et al., 2020, ApJ, 901, 166
van't Hoff M. L. R., Ohashi N., Jørgensen J. K., Tobin J. J., in prep., ApJ